Ceramics

Conductivity, microstructure and mechanical properties of tape-cast LATP with LiF and SiO$_2$ additives

Jürgen Peter Gross[1,*] , Jürgen Malzbender[1], Enkhtsetseg Dashjav[2], Frank Tietz[2,3], and Ruth Schwaiger[1,4]

[1] *Forschungszentrum Jülich GmbH, Institute of Energy and Climate Research, Microstructure and Properties of Materials (IEK-2), 52425 Jülich, Germany*

[2] *Forschungszentrum Jülich GmbH, Institute of Energy and Climate Research, Materials Synthesis and Processing (IEK-1), 52425 Jülich, Germany*

[3] *Forschungszentrum Jülich GmbH, Helmholtz-Institute Münster (IEK-12), 52425 Jülich, Germany*

[4] *Chair of Energy Engineering Materials, RWTH Aachen University, 52056 Aachen, Germany*

ABSTRACT

LATP sheets with LiF and SiO$_2$ addition prepared by tape cast as electrolytes for solid-state batteries were characterized regarding conductivity, microstructure and mechanical properties aiming toward an optimized composition. The use of additives permitted a reduction of the sintering temperature. Rietveld analyses of the samples with additives revealed a phase mixture of NaSICON modifications crystallizing with rhombohedral and orthorhombic symmetry as a superstructure with space group Pbca. It seems that LiF acts as a sintering additive but also as a mineralizer for the superstructure of LATP. As general trend, higher LiF to SiO$_2$ ratios led to lower porosities and higher values of elastic modulus and hardness determined by indentation testing, but the presence of the orthorhombic LATP leads to a decrease in the ionic conductivity. Micro-pillar testing was used to assess the crack growth behavior revealing weak grain boundaries.

Introduction

Batteries are considered a key technology for the transportation sector and storage of renewable energy [1]. Therefore, in recent years, a large number of studies have concentrated on the development of next generation battery technologies. They focused mainly on two aspects: the optimization of current batteries and the development of new materials for next-generation batteries, especially all-solid-state batteries [2], where in particular materials possessing

Springer

the NaSICON (Na$^+$ Super Ionic CONductors) structure are considered to be promising solid electrolytes [3, 4].

In particular, for the application in all-solid-state lithium batteries, $Li_{1+x}Al_xTi_{2-x}(PO_4)_3$ (LATP) with the NaSICON structure is a favorable material due to high ionic conductivity [5]. However, issues related to crack formation or delamination of interfaces can deteriorate material properties and battery performance [1]. In fact, a large number of publications are available on different synthesis approaches and resulting conductivities of LATP [6–15], but only a limited number of publications have addressed the failure-relevant mechanical properties of solid electrolytes [6, 16–20].

In general, to warrant reliable operation, ceramic materials should not change properties due to operation, deform only elastically and be resistant to crack growth [21]. Hence, especially the characterization of the elastic modulus and the crack growth behavior is important. Additional challenges arise for tape-cast solid electrolytes. This processing route promises to fulfill the requirements of large-scale fabrication, reduced costs and thin separators [22]. The limited thickness, though, complicates the determination of the mechanical properties [23], in particular of the fracture toughness K_{IC}, which is frequently based on the Vickers indentation testing [24]. However, Sebastiani et al. [24, 25] established a micro-pillar indentation splitting method that can facilitate the determination of the local fracture toughness. This method was already successfully used to determine the intragranular fracture toughness of LATP by testing micro-pillars prepared within large grains [20]. In order to determine the resistance of the solid electrolyte against lithium dendrite formation and growth, though, potential effects of intergranular and transgranular crack growth on the fracture toughness must also be considered [1].

Generally, impurities in LATP specimens segregate at the grain boundaries, thus blocking the transport of Li$^+$ ions [26]. While the usage of sintering additives might seem counter-intuitive, we could show in our previous work [27] that the inhibition of grain growth and crack formation in LATP can be achieved by adding 1.5 wt.-% SiO$_2$. This additive also allowed a reduction of the sintering temperature to 920 °C (compared to 970 °C for pure LATP) and a higher densification. The right combination and concentration of additives as well as precisely adjusted

sintering conditions are therefore needed in order to obtain improved LATP material. Therefore, aiming toward optimization, in this work a combination of SiO$_2$ and LiF was added in the synthesis of LATP. The addition of LiF is expected to lead to improved grain boundaries, higher relative densities and should compensate a possible Li loss [28–30].

Pure LATP as well as specimens with LiF and SiO$_2$ additives was prepared by tape casting. Their sintering behavior was investigated by dilatometry. The ionic conductivity was measured by impedance spectroscopy, and the microstructure was analyzed using scanning electron microscopy. Elastic modulus and hardness of the specimens were characterized using different indentation methods. The fracture toughness was estimated from the splitting of focused ion beam (FIB)-fabricated micro-pillars.

Experimental

A solution-assisted solid-state reaction was used to prepare LATP powder as described in detail elsewhere [31, 32]. Subsequently, the powder was calcined at 700 °C for 4 h. The resulting material was ball-milled for 24 h in ethanol using ZrO$_2$ balls, then dried for 24 h at 70 °C and mortared. The particle size distribution in ethanol suspension was measured by laser scattering analysis (Horiba LA 950 V2) using the Fraunhofer scattering approximation [33]. The specific surface area was measured according to the Brunauer–Emmett–Teller (BET) method with nitrogen gas. The obtained powder had a mean particle size, D_{50}, of 0.78 µm and a specific surface area of 15.23 m^2 g^{-1}.

In a previous work [27], 1.5% of an amorphous SiO$_2$ nano-powder (Alfa Aesar) was used as sintering additive to improve conductivity and mechanical properties of electrolyte sheets. Here, different ratios of SiO$_2$ and LiF varying from 1:1.5 to 1:4 (summarized in Table 1) were used to improve sinterability, ionic conductivity and mechanical properties.

The slurry for the tape-cast process was prepared by dispersing LATP in a mixture of ethanol and methyl-ethyl-ketone (34:66 vol.-%). Polyvinylbutyral as a binder (6.3 wt.-% with respect to LATP, Butvar B-98), Nousperse FX9086 as a dispersant (3.6 wt.-% with respect to LATP, Elementis Specialties), polyethylene glycol (3.5wt% with respect to LATP, PEG400) and Solusolv S-2075 (3 wt.-% with respect to

Table 1 Targeted compositions of the samples

Sample	LiF-addition [wt.-%]	SiO$_2$-addition [wt.-%]	Ratio
LATP:Pure	0.0	0.0	–
LATP:1.5F0.5Si	1.5	0.5	3:1
LATP:1.5F1Si	1.5	1.0	1.5:1
LATP:2F0.5Si	2.0	0.5	4:1

LATP, Solutia Inc.) as plasticizers and as sintering additives, SiO$_2$ (0–1.0 wt.-% with respect to LATP, Alfa Aesar) in combination with LiF (0–2 wt.-%, Alfa Aesar) were added to the mixture (see Supplementary Material for further details). Using a high energy planetary mill (Thinky ARV-310) with ZrO$_2$ balls, the mixtures were homogenized and dispersed for 5 min at 1500 rpm. Subsequently the slurries were polymerized at room temperature for 48 h without rotation, degassed at 20 kPa for 10 min and then cast using a tape-cast machine (KARO cast 300–7, KMS Automation GmbH, Germany) with a slit height of 350 μm at a drawing speed of 3.5 mm/s.

In order to determine the optimal sintering temperature, the sintering behavior of the tape-cast green sheets was analyzed by a pushrod dilatometer (DIL 402C, Netzsch) in contact mode, with a force of 200 mN. Green tapes of 1 cm^2 and approximately 1 mm thickness were clamped horizontally between alumina rods, and their thickness changes versus temperature up to 950 °C with 5 K/min heating rate in dry air were recorded. The cast foils were dried and cut into circular discs of 16 mm diameter and sintered in air at different temperatures for 4 h, resulting in 90–110-μm-thick sheets. Fragments of the sintered LATP discs were ground in a mortar. The powder was dispersed in ethanol and applied onto a silicon zero-background sample holder. X-ray diffraction (XRD) data were collected with an EMPYREAN diffractometer (Malvern Panalytical, Eindhoven, Netherlands) using Cu-Kα radiation. Data analysis employing the Rietveld method for determining lattice parameters and phase fractions was carried out using the software package TOPAS version 6 (Bruker AXS, Karlsruhe, Germany).

In order to measure the ionic conductivity, the surfaces were sputtered with gold on both sides and placed into an electrochemical cell (EL-CELL, PAT-Cell) under Ar atmosphere. The impedance spectra were measured using a potentiostat (Bio-Logic, SP-300) in the frequency range of 7 MHz to 1 Hz with 20 mV sinus amplitude at room temperature.

The samples for the subsequent microstructural and mechanical characterization were embedded in water-free epoxy resin and manually polished using 400 to 4000 SiC grinding papers. The fine polishing was conducted with a Minimet® 100 polisher using water-free diamond suspensions with grain sizes from of 4 μm down to 1 μm. The final polishing was conducted using water-free colloidal silica polishing solution with a grain size of 0.2 μm. For LATP, the water-free sample preparation was necessary to prevent a reaction with water [34, 35].

Scanning electron microscopy (SEM) images were obtained using a Zeiss Merlin SEM (Carl Zeiss Microscopy, Oberkochen, Germany). The porosity was estimated based on the analysis of SEM micrograph following the specifications outlined in [36], where pores are identified based on the gray-scale-level. The corresponding manual thresholding was carried out using the software ImageJ [37]. At least six SEM images of different locations on the specimens surface were analyzed for each sample.

A piece of LATP:1.5F0.5Si was fixed between two pieces of a Si wafer with epoxy resin for microstructural studies and element identification. A cross-section of this assembly was first mechanically ground using 800 SiC grinding paper, followed by Ar ion milling at 6 kV for 8 h using a SM-09010 Cross-Section Polisher (Jeol, Tokyo, Japan). Energy-dispersive X-ray (EDX) maps and spectra were recorded for this specimen using X-Max Extreme and X-Max 80 EDX detectors (Oxford Instruments, High Wycombe, UK) fitted to the SEM. The Oxford Instruments Aztec software was used for data acquisition and processing. EDX maps were recorded at an acceleration voltage of 5 kV with the X-Max Extreme detector, and EDX spectra of single grains/particles were collected at 10 kV with the X-Max 80 detector.

Elastic moduli E and hardness values H were determined from indents into the surface of the

embedded and polished samples using a FISCHER-SCOPE® HC 100 instrument (Helmut Fischer GmbH, Sindelfingen) equipped with a Vickers diamond tip. The samples were indented to a load of 30 mN to measure the average intrinsic properties of the materials [34]. On each specimen, at least 100 indentations were performed with a load application time of 15 s and a hold period of 1 s before unloading the sample. The values of E and H were determined from the unloading slope of the load–displacement curve following the DIN EN ISO 3452–1 standard. A Poisson ratio of 0.25 was assumed for all materials [16]. In addition, some indentations were carried out at higher loads using a CSM indenter (Anton Paar CSM Micro-Indentation Tester, Peseux, Switzerland) to test the feasibility of measuring the indentation fracture toughness with a Vickers tip; loads of 50, 300 and 500 mN with loading rates of 30 N/h were applied.

A micro-pillar splitting method was used to estimate effects of intergranular and transgranular crack growth on the fracture toughness of LATP. Micropillars were fabricated by focused ion beam (FIB) cutting using an Auriga cross-beam instrument (Carl Zeiss Microscopy, Oberkochen, Germany) operated at an acceleration voltage and beam currents of 30 kV and 2–16 nA, respectively. In order to minimize any potential influence of FIB damage on K_{IC}, the diameter of the pillars should be 10 μm or larger [38]. Therefore, for each specimen 5 pillars with a target diameter of 10 μm were cut. For the pillar-splitting test, a ratio of $z/D \sim 1$ is required [24], where D is the diameter and z the height of the pillar. Hence in the current work, pillars with 10 μm in diameter and 10 μm in height were tested.

For each pillar, topographic images were recorded in order to confirm the pillar geometry using a laser confocal LEXT OLS6000 microscopy instrument (OLYMPUS, Hamburg, Germany) employing a step size of 0.2 μm. The positioning of the indenter tip in the center of the pillars was ensured and errors due to indenter positioning can be neglected [38]. Subsequently load-controlled indentation tests were performed at a load rate of 0.5 mN/s to split the pillars using a NanoXtrem nanoindenter (Micro Materials, Wrexham, UK) equipped with a Berkovich type diamond tip.

Results and discussion

Although the amount of sintering additives was ≤ 3 wt.-% in all cases, the sintering behavior of LATP samples was strongly affected by the additives. Figure 1 presents the sintering behavior in terms of the measured shrinkage of the samples from room temperature to 950 °C at a constant heating rate of 300 K/h. The two samples with 1.5% LiF and different amounts of SiO_2 exhibited very similar shrinkage curves compared to the sample with 2% LiF. The shrinkage at 815 °C for the samples LATP:1.5F0.5Si and LATP:1.5F1Si was 24% and 26%, respectively (see Fig. 1). Below 700 °C, no dimensional change could be observed.

According to the dilatometer curves, the LATP sample without sintering additive started to shrink slowly at around 800 °C and reached 22% shrinkage at 950 °C. For the samples with additives, the onset points of shrinkage decreased toward 750 °C followed by a sharp increase in shrinkage rate to reach a maximum shrinkage at around 880 °C. This corresponded to an almost 130 °C reduction in the sintering temperature compared to pure LATP. In the case of the LATP:2F0.5Si sample, the onset of the sintering was similar to that of the others, however, the total shrinkage was lower (approximately 20%). The length expansion at temperatures above 850 °C of the three samples containing LiF and SiO_2 is caused by the melting [39] and slowly increasing evaporation rate of LiF.
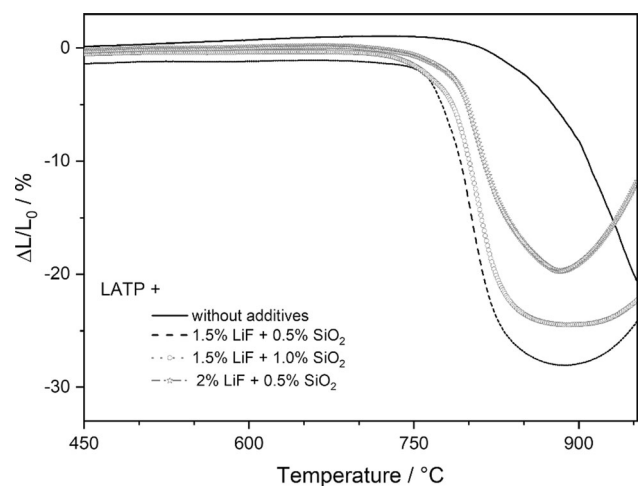

Figure 1 Length change of different LATP samples as a function of temperature determined by dilatometry. The shrinkage behavior is affected by the amount of sintering additives.

As shown previously [27], single-phase LATP can be obtained at sintering temperatures above 900 °C. In this work, almost single-phase LATP could be obtained without additives via sintering at 940 °C, in agreement with the previous work. For the samples with additives, the sintering temperature could be reduced to 815 °C. Phase analysis employing Rietveld refinements was carried out in order to check for the presence of additional phases, such as TiO_2, $AlPO_4$ or other NaSICON-related structures. The XRD patterns of the samples with SiO_2 and LiF additives contain the rhombohedral NaSICON-type LATP (space group $R\overline{3}c$, ICSD no. 7936) and the $LiTiOPO_4$ minority phase (space group Pnma, ICSD no. 153522). Additional peaks could be fitted using a model with an orthorhombic superstructure of the NaSICON-structure (space group Pbca, $Li_2Mn_2(SO_4)_3$ type, ICSD no. 51332 for $Li_2Fe_{1.075}Ti_{0.925}(PO_4)_3$ [40]) where Fe might be replaced by Al. The actual composition of both phases, i.e., the Ti/Al ratio, could not be reliably determined based on the XRD data. In order to obtain comparable results for all samples, structural parameters such as atomic positions, site occupation factors and temperature factors were kept constant during the refinement. For simplicity, the two LATP phases are labeled LATP-1 (rhombohedral NaSICON) and LATP-2 (orthorhombic NaSICON superstructure). The reflection profiles of both LATP-1 and LATP-2 are significantly wider compared to the pure LATP sample, which is caused by micro-strain rather than small domain sizes. In addition, the reflection line broadening of the LATP-2 phase is anisotropic due to different domain sizes in different crystallographic directions. Such anisotropy is typically observed in the case of micro-twinning and has been considered in the course of the lattice parameter refinement. The results of the Rietveld refinement are summarized in Table 2. Figure 2 shows the measured and Rietveld refined XRD patterns of pure LATP and LATP:1.5F1Si (diagrams for LATP:1.5F0.5Si and LATP:2F0.5Si are given in the Supplementary Material).

Rietveld refinement shows that the amount of the minority phase $LiTiOPO_4$ is around 3 wt.-% in the LATP:Pure sample and increases to around 10 wt.-% in the samples with SiO_2 and LiF additives. LATP-2 turns out to be the majority phase in the latter samples, while it is absent in LATP:Pure. Two factors can be considered as reason for the formation of the LATP-2 phase. First, the sintering temperature of the samples is lower, and secondly, the LiF may act as mineralizer for LATP-2. However, EDX analyses show that neither Si nor F is incorporated into the LATP phases in significant amount. Further work is necessary to clarify the formation conditions of the LATP-2 phase. The unit cell volume of LATP-1 in the samples with additions is increased only slightly (by less than 0.2%) compared to the LATP:Pure, which might be a result of peak overlap with the LATP-2 phase rather than caused by different composition. The values of the lattice parameters of the LATP-2 phase are slightly smaller than the reported data of $Li_2FeTi(PO_4)_3$ [40].

The Nyquist plots of the impedance spectra are shown in Fig. 3. The equivalent circuit model for fitting and dimensions of measured samples are given in Fig. 3. For each sample, one semi-circle at high frequencies along with an inclined spike at low frequencies is observed. The fitted resistance at the left intercept of the semi-circle is taken as bulk resistance (R_b) and the right intercept as total resistance. These conductivities are obtained using the equation: $\sigma_{total} = t / R \cdot A$, where t and A are thickness of the disk and electrode area, respectively (Table 3).

The fitting model resembles the bulk resistance (R_b), grain boundary resistance (R_{gb}) in parallel combination with a constant-phase element CPE_{gb} and a constant-phase element CPE_{EL} related to the electrode polarization. The impedance of the constant-phase element is given as $Z_{CPE} = \frac{1}{Q} \cdot (i\omega)^{-n}$ with $n \le 1$. Effective capacitances were calculated using $C_{eff} = Q^{1/n} R^{(1-n)/n}$ [41]. For the effective capacitance of the bulk, we used the value of $4 \cdot 10^{-10}$ F cm^{-2} from our former work [27]. The grain boundary capacitancies for the four samples are much larger and vary from $1 \cdot 10^{-8}$ F cm^{-2} to $4 \cdot 10^{-7}$ F cm^{-2}. Considering the values of C_b and C_{gb}, the grain boundary conductivity can be calculated with the equation $\sigma_{gb} = t/A \cdot (C_b/C_{gb}) \cdot (1/R_{gb})$ [42], which is also listed in Table 3, along with sintering temperature, sample thickness and corresponding porosity. The pure LATP sample showed the highest total ionic conductivity of 0.87 mS/cm, grain boundary conductivity of 0.70 mS/cm and bulk conductivity of 2.55 mS/cm. The total and grain boundary conductivity are very close in the magnitude, whereas the bulk conductivity is in very good agreement with 3 mS/cm from single crystal data [43].

Table 2 Lattice parameters and Rietveld refinement statistics of the phases in the investigated samples

Phase	Sample	LATP:Pure	LATP:1.5F0.5Si	LATP:1.5F1Si	LATP:2F0.5Si
$R\bar{3}c$	a [Å]	8.488	8.474	8.474	8.473
LATP1	c [Å]	20.768	20.850	20.859	20.863
ICSD 7936	V [Å^3]	1295.91	1296.76	1297.26	1297.17
	wt.-%	96	42	42	36
Pbca	a [Å]	–	8.460	8.461	8.460
LATP2	b [Å]	–	8.523	8.523	8.525
ICSD 51,332	c [Å]	–	23.792	23.794	23.792
	V [Å^3]	–	1715.4	1715.9	1715.8
	wt.-%	–	50	50	53
$LiTiOPO_4$	a [Å]	7.400	7.398	7.399	7.400
ICSD 153,522	b [Å]	6.374	6.371	6.372	6.371
	c [Å]	7.232	7.237	7.239	7.240
	V [Å^3]	341.11	341.15	341.33	341.33
	wt%	4	8	8	10
Refinement	GOF,	1.96,	3.56,	3.56,	3.67,
statistic	R_{exp}, R_{wp}	1.55, 3.03	1.87, 6.65	1.92, 6.82	1.86, 6.83

For three samples with sintering additives, the total and grain boundary conductivities are almost one order magnitude lower than that of pure LATP, ranging between σ_{tot} = 0.03 mS/cm and 0.15 mS/cm and σ_{gb} = 0.06–0.13 mS/cm, respectively. The results in Table 3 clearly show that the sintering additives have an impact on both the bulk and the grain boundary conductivity, indicating that especially the SiO_2 addition seems to influence the ionic conductivity negatively. The reduced bulk conductivity is probably caused by the increased amount of the $LiTiOPO_4$ minority phase, and especially the presence of the LATP-2 phase with NaSICON superstructure. The ionic conductivity of LATP-2 is hitherto unknown and needs to be characterized in future studies.

Representative SEM micrographs are shown in Fig. 4. The addition of SiO_2 and LiF led to a reduced porosity compared to the pure LATP sample (Fig. 4a). Although mostly grain boundaries could not be identified, the grain size was probably smaller than the distance between the pores, thus, below 2 μm. However, in certain regions of the specimens individual grains can be seen confirming the estimated grain size of < 2 μm (see Supplementary Material).

The porosity decreased for the specimens with LiF and SiO_2 additives compared to the pure LATP. The additives reduced the porosity from 14.7 ± 2.5% for the pure LATP to 5.8 ± 0.4% for the LATP specimens with an addition of 2 wt.-% LiF and 0.5 wt.-% SiO_2.

The pore sizes of the specimens with additives were comparable consisting of small (< 0.5 μm) and larger (~ 1 μm) pores, whereas in the pure LATP only small pores were observed.

In order to check the distribution of the additives, and in particular the incorporation of Si or F into the LATP phase, EDX analysis was carried out on an Ar-ion polished cross section of LATP:1.5F1Si. This preparation route avoids any external Si sources such as SiC grinding paper or SiO_2-containing polishing media and yields high-quality surfaces suitable for low-energy EDX analysis. EDX maps of an area that is particularly rich in minority phases shown in Fig. 5 reveal the presence of $LiTiOPO_4$, SiO_2 and a phosphate-rich phase besides the LATP-1 and LATP-2 majority phases. The phosphate-rich phase is present inside pores between the LATP grains. It cannot be identified because it decomposes under the electron beam. Furthermore the regions of this phase are too small to exclude matrix contributions in the EDX spectrum. SiO_2 was mainly found as discrete particles between the LATP grains and occasionally enclosed in LATP grains, whereas F had been incorporated into the central regions of $LiTiOPO_4$ grains together with Al. The LATP-1 and LATP-2 phases identified by XRD analyses are expected to have different Ti/Al ratio, which is confirmed by the intensity variation in the Al map. The Ti signal is too weak to observe a corresponding variation in the Ti map.

The EDX maps (Fig. 5) do not indicate incorporation of significant amounts of Si or F into the LATP

Figure 2 Rietveld refinements for the two samples **a** LATP:Pure and **b** LATP:1.5F1Si.
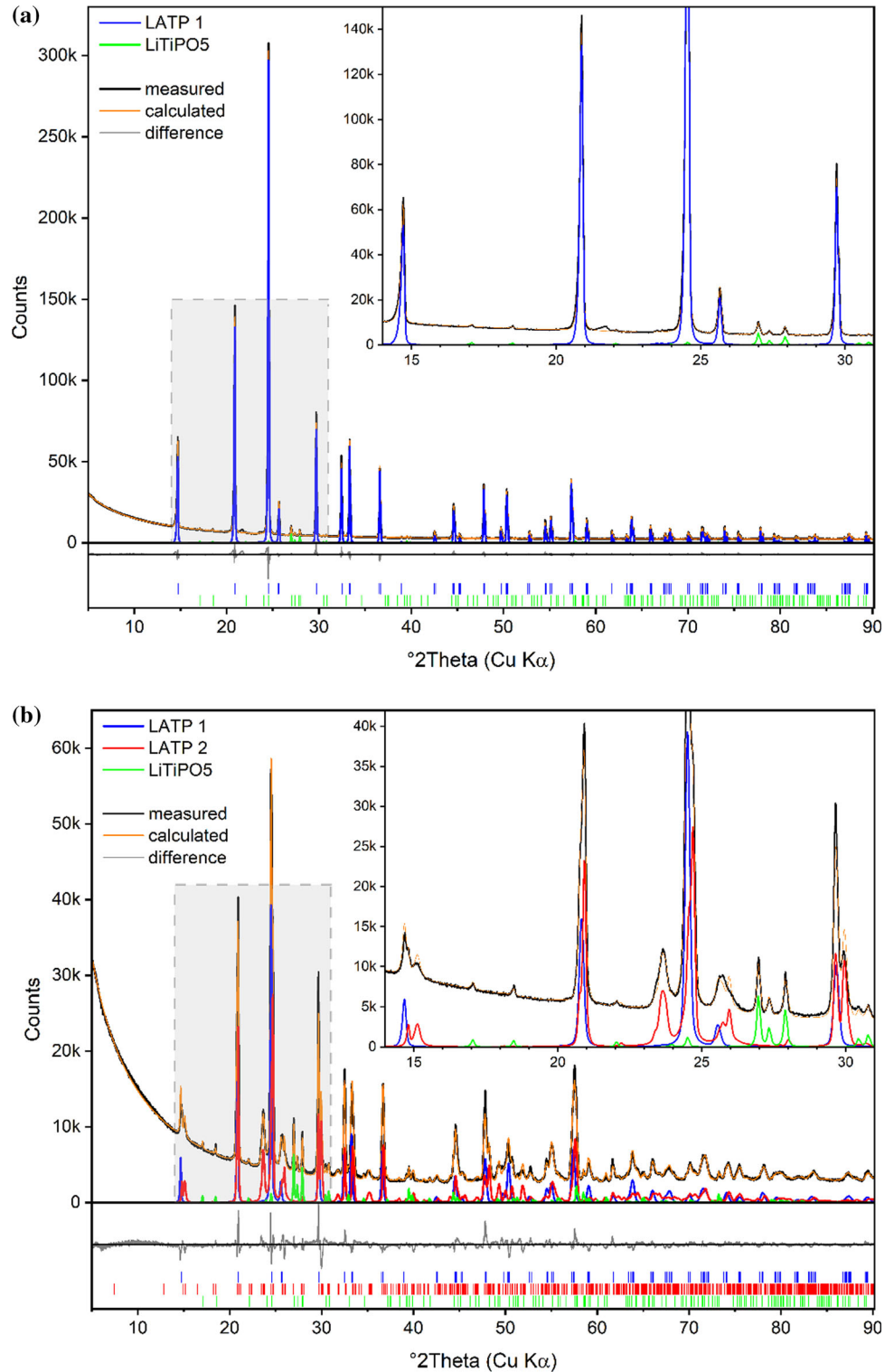
phase. In order to check for small amounts of F or Si, additional EDX spectra were recorded (see Supplementary Material). The EDX spectrum of LATP shows a weak Si-K emission peak, while the F-K peak is absent, whereas the spectrum of LiTiOPO$_4$ shows a similarly weak Si-K peak and a clear F-K peak in agreement with the EDX maps. The content of F in the center of the analyzed grain corresponds to 1–2 wt.-%. The amount of Si in both phases is similar and
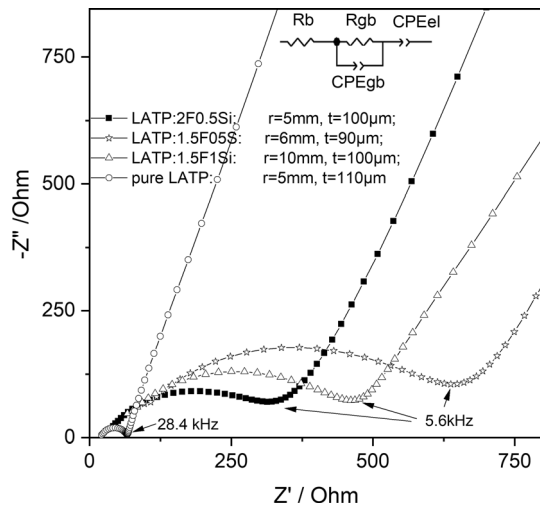
Figure 3 Nyquist plot of the investigated samples.

close to the limit of detection of EDX spectroscopy, approximately 0.2 wt.-%.

Figure 6a, b shows an enhancement of the elastic moduli and hardness values for the specimens with SiO_2 as well as the LiF addition compared to the pure LATP sample. For pure LATP, elastic moduli ranging from 81 to 115 GPa have been reported [44], whereas the average value for pure LATP obtained in this work is 64 ± 5 GPa and, thus, significantly lower. The elastic moduli of the specimens with LiF and SiO_2 addition are between ~ 94 and ~ 106 GPa and therefore well within the range reported for pure LATP. The hardness value reported in the literature for pure LATP is 7.1 ± 1.0 GPa [44]. However, here pure LATP revealed a much lower hardness of 2.9 ± 0.6 GPa, while for the material with LiF and SiO_2 addition the hardness values vary between ~ 8.4 and ~ 11.4 GPa. As mentioned above, the additives have a significant effect on the porosity, which needs to be considered in the interpretation of the data obtained from the indentation tests. Thus, in Fig. 6c, d the elastic modulus and hardness data are presented as a function of the porosity, revealing that

both properties are significantly affected by the porosity. The impact of porosity on the elastic modulus of materials is already known, and a number of different models have been proposed in order to explain this dependency [45–48]. The occurrence of LATP2 phase might also impact the mechanical properties of the specimens, but different phases cannot be distinguished in the indentation testing. Furthermore, the porosity influence seems to be the dominating factor concealing any possible influence of the LATP2 phase.

In order to assess whether the frequently used measurement of radial or Palmqvist type cracks is applicable here i.e., to learn whether the properties obtained for such thin specimens are affected by the low compliance of the embedding material, Vickers indentations were carried out on a LATP:2F0.5Si specimen. The resulting elastic modulus and hardness values decreased significantly with increasing load due to the deformation of the embedding material (see Supplementary Material), thus, ruling out the use of this method.

A typical micro-pillar prior to testing is shown in Fig. 7. The pillar size is much larger than the grain size. Furthermore, the polycrystalline nature of the pillars can clearly be seen. The surface was not perfectly flat due to the porosity and an angle of approximately 15° existed between the side walls and the surface normal, as determined by laser confocal microscopy. In addition, the top surface of the pillars was slightly elliptical rather than circular and the edges were slightly rounded. However, such imperfections have also been reported in other studies for FIB-milled micro-pillars and it has been shown that any potential influence on the results decreased with increasing pillar size, i.e., being insignificant for the pillar sizes used in this work [35].

Representative images of the micro-pillars after the indentation testing are shown in Fig. 8. Figure 8a shows a deformed micro-pillar of specimen LATP:

Table 3 Sintering temperature T_{sint}, thickness t, resistivity R, ionic conductivity σ and porosity

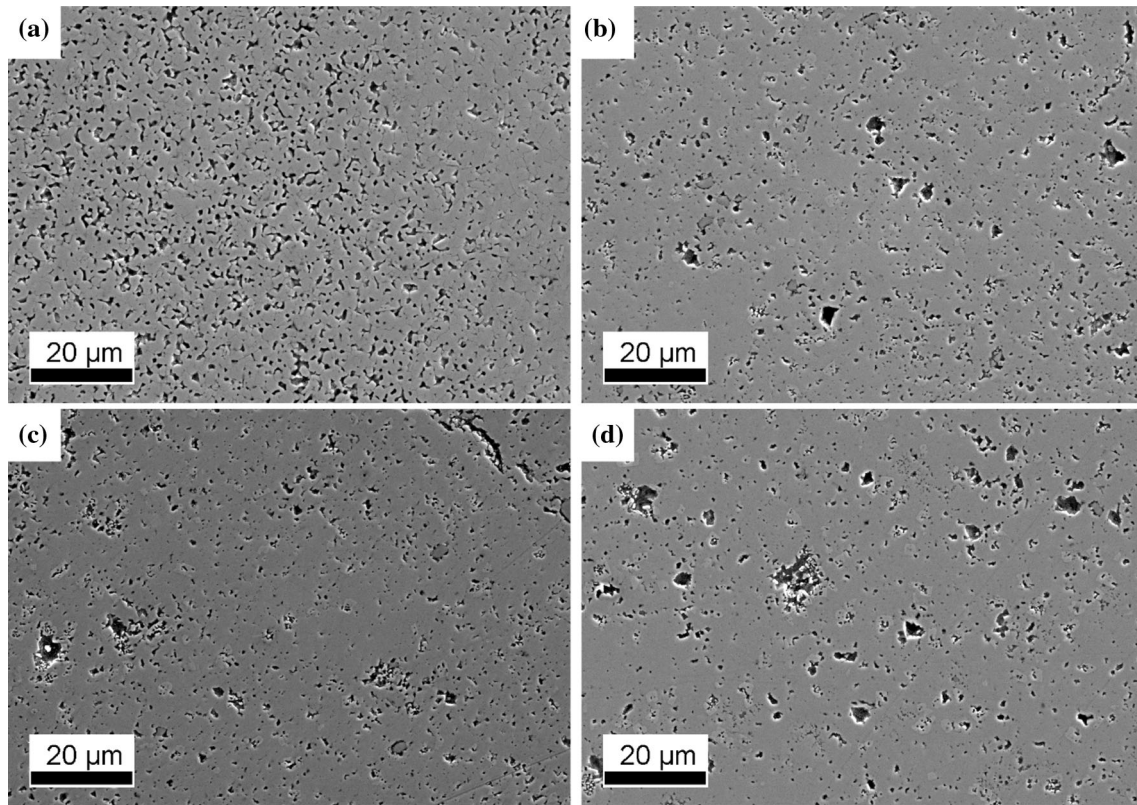| Sample name	T_{sint} [°C]	t [μm]	A [cm²]	Resistivity, R [Ω]		Conductivity, σ [mS/cm]			Porosity [%]
				R_b	R_{gb}	σ_b	σ_{gb}	σ_{total}	
LATP:Pure	940	110	0.196	22	42.25	2.55	0.70	0.87	14.7 ± 2.5
LATP:1.5F0.5Si	815	90	0.283	47.7	636.6	0.67	0.12	0.05	8.7 ± 0.9
LATP:1.5F1Si	815	100	0.785	36.13	428.8	0.35	0.06	0.03	7.3 ± 1.0
LATP:2F0.5Si	820	100	0.196	24.57	323.4	2.07	0.13	0.15	5.8 ± 0.4

Figure 4 SEM micrographs of **a** LATP: pure, **b** LATP:1.5F0.5Si, **c** LATP:1.5F1Si and **d** LATP:2F0.5Si.
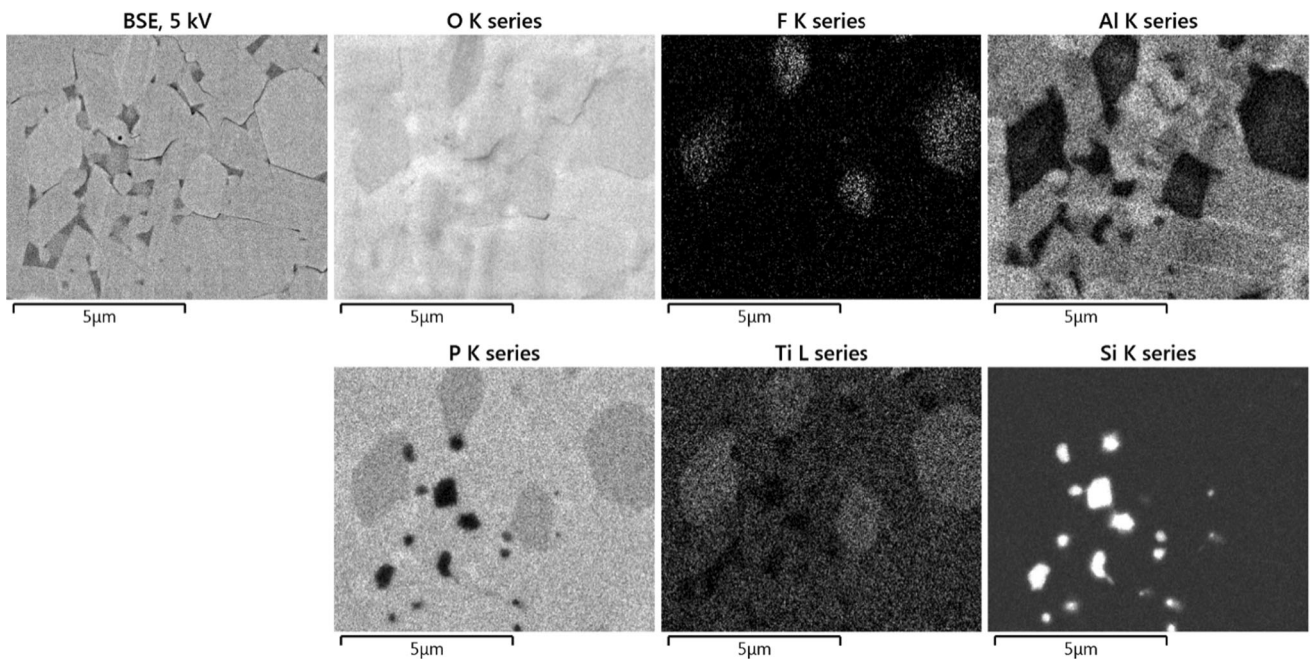

Figure 5 EDX mapping results for the LATP:1.5F1Si specimen.

Pure. The indenter tip displaced the grains rather than deforming them due to the high porosity, therefore a clear imprint is not visible. The displacement of the grains led to secondary cracks along the grain boundaries indicating weak grain boundaries. When the load was further increased,
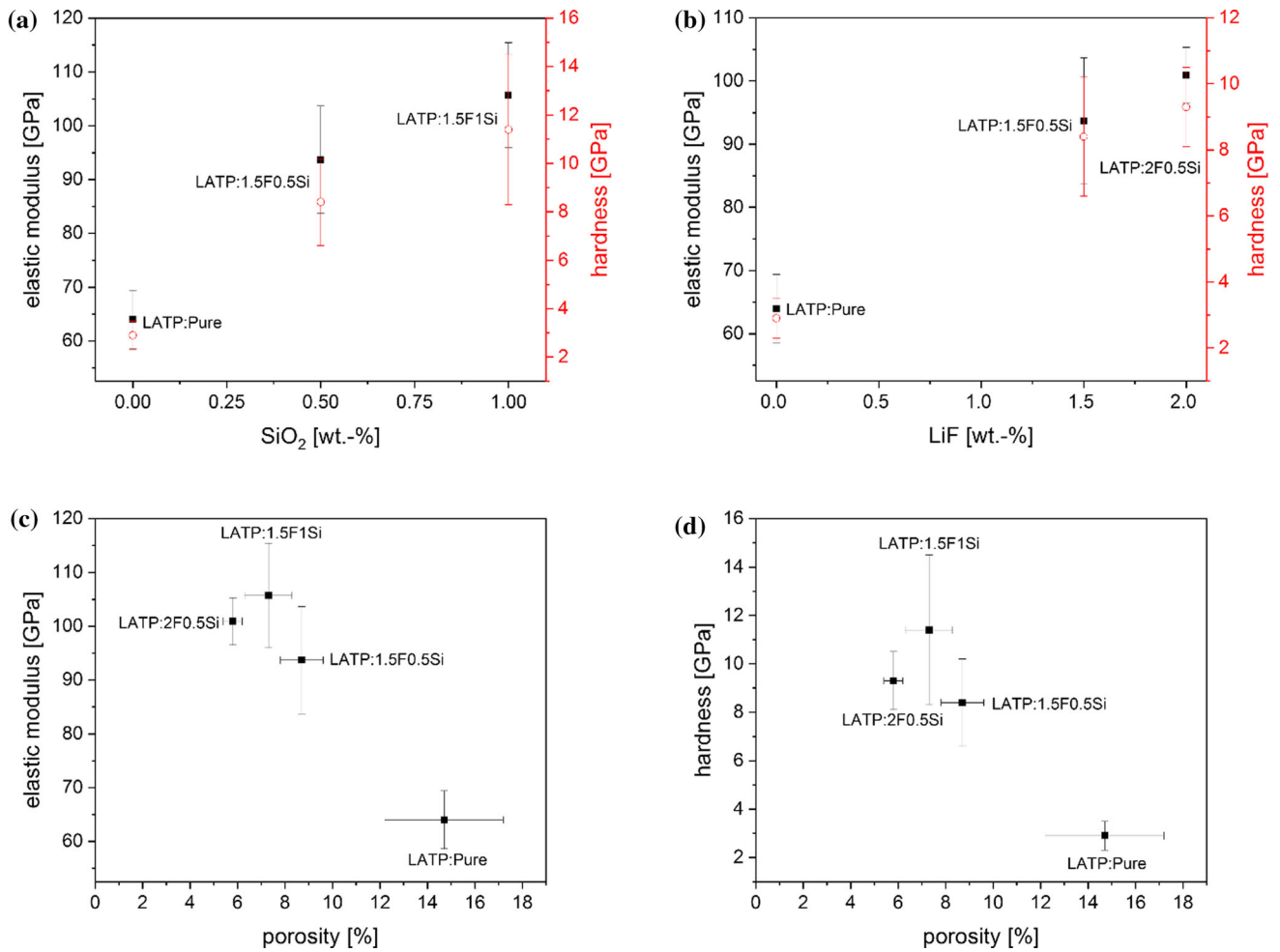
Figure 6 Elastic moduli (load of 30 mN) determined by indentation tests as a function of the **a** SiO$_2$ addition and **b** LiF addition. **c** Elastic modulus and **d** hardness values as a function of the porosity.
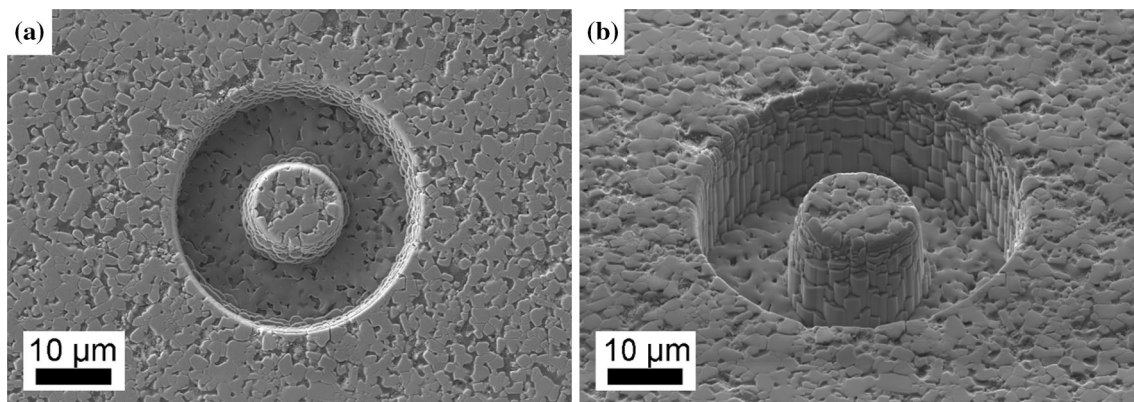
Figure 7 SEM micrographs of a 10 μm pillar in LATP:1.5F1Si before testing, **a** top view and **b** side view (at 56° tilt angle).

beyond the apparent critical load, the micro-pillar rather disintegrated into a pile of individual grains instead of being clearly crushed, as shown in Fig. 8b. This observation underscores the presence of weak

grain boundaries. By contrast, the micro-pillars of the sample LATP:1.5F0.5Si showed an indentation imprint after testing. The crack origin seems to be located in the vicinity of the corners of the imprints,
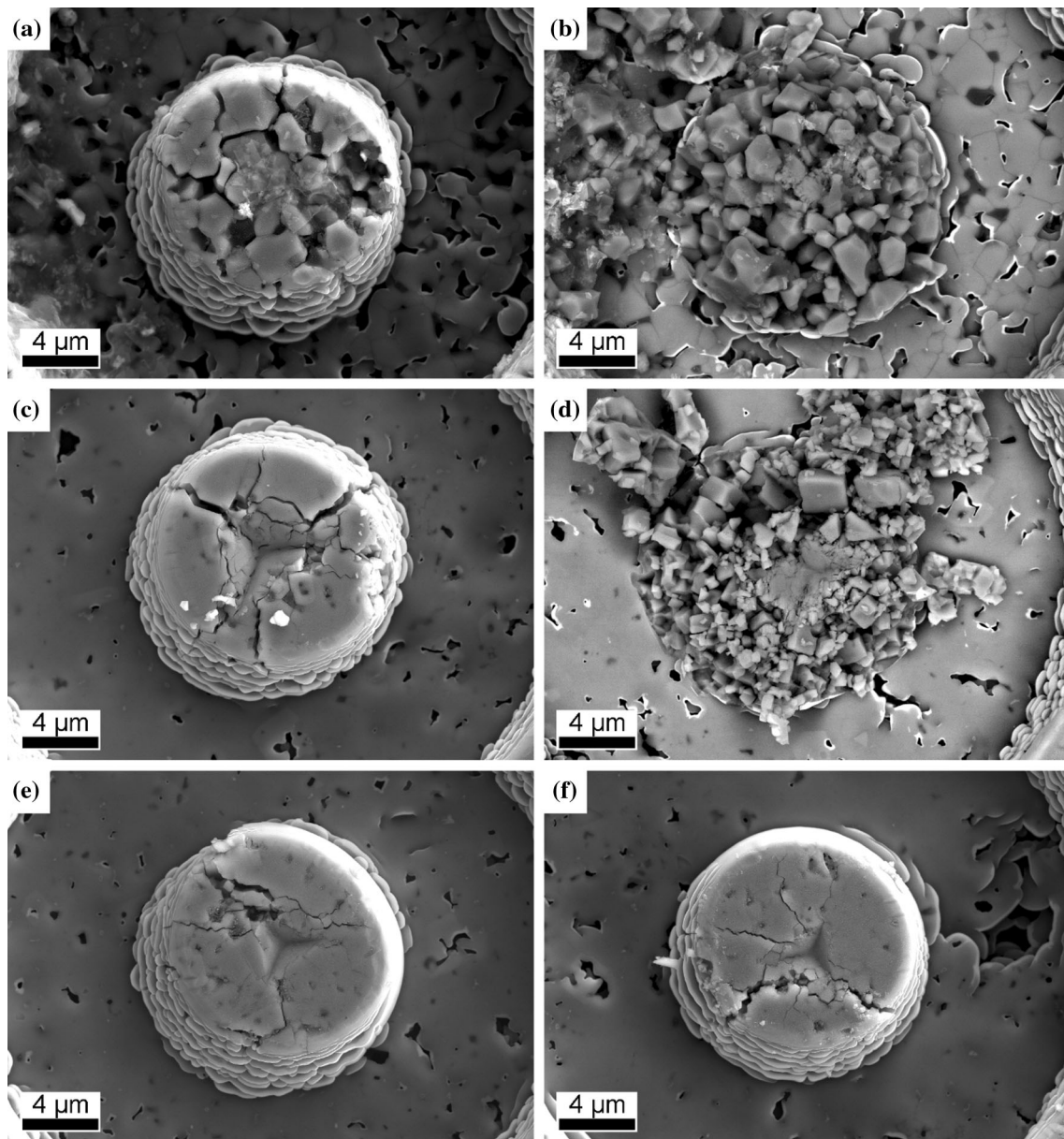
Figure 8 Representative SEM micrographs of micro-pillars after the micro-pillar splitting test of the different materials LATP:Pure (**a**, **b**), LATP:1.5F0.5Si (**c**, **d**), LATP:1.5F1Si (**e**) and LATP:2F0.5Si (**f**).

while small deviations might be explained by pores at the surface of the pillars. Secondary cracks can be observed, although it is unclear whether they were induced during the loading or rather upon unloading of the tip. Again, the cracks seem to propagate along the grain boundaries indicating intergranular fracture. An increase in the load beyond the critical load also leads to disintegration of the micro-pillar, as shown in Fig. 8c, d. The specimens LATP:1.5F1Si and LATP:2F0.5Si behave similarly in the micro-pillar test. For both specimens, a crack formed parallel to the edge of the imprint, which seems to originate from pores located at the micro-pillar surface and to propagate along the grain boundaries (Fig. 8e, f). This behavior is consistent for all micro-pillars of these two samples. The results clearly show that the grain boundaries need to be improved. Based on the equations given in [24], fracture toughness values can be estimated in the range of 0.2–0.4 MPa m$^{1/2}$.

Conclusion

In this work, the influence of LiF and SiO_2 additions on the apparent ionic conductivity, microstructure and mechanical properties of sintered tape-cast LATP sheets, with thicknesses of around ~ 100 µm, has been investigated. The use of LiF and SiO_2 additives allowed a reduction in the sintering temperature and a reduction in the porosity. In addition, the ionic conductivity decreased compared to pure LATP despite a reduction in the porosity due to the increased amount of minority phases and the presence of the orthorhombic NaSICON phase (LATP-2) in the samples with additives. Neither of the additives is incorporated into the LATP phases in significant amounts.

The highest elastic moduli and hardness values were observed for LATP:1.5F1Si and LATP:2F0.5Si. However, the results were significantly affected by the porosity. A further reduction in the porosity of tape-cast LATP would certainly improve the physical and mechanical properties, which might be achieved by an optimization of the LiF and SiO_2 sintering additives. Possible influences of the orthorhombic NaSICON phase on the mechanical properties are concealed by the dominating porosity impact.

A micro-pillar splitting technique was used to investigate the crack growth behavior. It was shown that the grain boundaries need to be improved, since intergranular crack propagation was observed and the micro-pillars disintegrated into individual grains.

Acknowledgements

Funding

References

[1] T. Famprikis, P. Canepa, J. A. Dawson, M. S. Islam, and C. Masquelier (2019) Fundamentals of inorganic solid-state electrolytes for batteries. *Nature materials*, pp. 1–14.

[2] Placke T, Kloepsch R, Dühnen S, Winter M (2017) Lithium ion, lithium metal, and alternative rechargeable battery technologies: the odyssey for high energy density. J Solid State Electrochem 21(7):1939–1964

[3] Goodenough JB, Hong H-P, Kafalas J (1976) Fast Na+-ion transport in skeleton structures. Mater Res Bull 11(2):203–220

[4] Hong H-P (1976) Crystal structures and crystal chemistry in the system Na1+ xZr2SixP3− xO12. Mater Res Bull 11(2):173–182

[5] Fu J (1997) Superionic conductivity of glass-ceramics in the system Li 2O-Al 2O 3-TiO 2-P 2O 5. Solid State Ionics 96(3–4):195–200

[6] Jackman SD, Cutler RA (2012) Effect of microcracking on ionic conductivity in LATP. J Power Sources 218:65–72

[7] Soman S, Iwai Y, Kawamura J, Kulkarni A (2012) Crystalline phase content and ionic conductivity correlation in LATP glass–ceramic. J Solid State Electrochem 16(5):1761–1766

[8] Kothari DH, Kanchan D (2016) Effect of doping of trivalent cations Ga3+, Sc3+, Y3+ in Li1. 3Al0. 3Ti1. 7 (PO4) 3

(LATP) system on Li+ ion conductivity. Physica B 501:90–94

[9] Duluard S et al (2017) Dense on porous solid LATP electrolyte system: Preparation and conductivity measurement. J Am Ceram Soc 100(1):141–149

[10] Kotobuki M, Koishi M (2013) Preparation of Li1. 5Al0. 5Ti1. 5 (PO4) 3 solid electrolyte via a sol–gel route using various Al sources. Ceram Int 39(4):4645–4649

[11] Kotobuki M, Koishi M, Kato Y (2013) Preparation of Li 1.5 Al 0.5 Ti 1.5 (PO 4) 3 solid electrolyte via a co-precipitation method. Ionics 19(12):1945–1948

[12] Bucharsky E, Schell K, Hintennach A, Hoffmann M (2015) Preparation and characterization of sol–gel derived high lithium ion conductive NZP-type ceramics Li1+ x AlxTi2− x (PO4) 3. Solid State Ionics 274:77–82

[13] Ma F et al (2016) Preparation and evaluation of high lithium ion conductivity Li1. 3Al0. 3Ti1. 7 (PO4) 3 solid electrolyte obtained using a new solution method. Solid State Ionics 295:7–12

[14] Morimoto H et al (2013) Preparation of lithium ion conducting solid electrolyte of NASICON-type Li1+ xAlxTi2− x (PO4) 3 (x= 0.3) obtained by using the mechanochemical method and its application as surface modification materials of LiCoO2 cathode for lithium cell. J Power Sources 240:636–643

[15] Kim KM, Shin DO, Lee Y-G (2015) Effects of preparation conditions on the ionic conductivity of hydrothermally synthesized Li1+ xAlxTi2-x (PO4) 3 solid electrolytes. Electrochim Acta 176:1364–1373

[16] Deng Z, Wang Z, Chu I-H, Luo J, Ong SP (2016) Elastic properties of alkali superionic conductor electrolytes from first principles calculations. J Electrochem Soc 163(2):A67–A74

[17] Nonemacher JF, Naqash S, Tietz F, Malzbender J (2019) Micromechanical assessment of Al/Y-substituted NASICON solid electrolytes. Ceram Int 45(17):21308–21314

[18] Yan G et al (2019) Influence of sintering temperature on conductivity and mechanical behavior of the solid electrolyte LATP. Ceram Int 45(12):14697–14703

[19] Cho Y-H, Wolfenstine J, Rangasamy E, Kim H, Choe H, Sakamoto J (2012) Mechanical properties of the solid Li-ion conducting electrolyte: Li 0.33 La 0.57 TiO 3. J Mater Sci 47:5970–5977. https://doi.org/10.1007/s10853-012-6500-5

[20] Yan G et al (2012) Fracture behavior of solid electrolyte LATP material based on micro-pillar splitting method. J Eur Ceram Soc 41(10):5240–5247

[21] Monroe C, Newman J (2005) The impact of elastic deformation on deposition kinetics at lithium/polymer interfaces. J Electrochem Soc 152(2):A396–A404

[22] Zhang M et al (2014) Solid state lithium ionic conducting thin film Li1. 4Al0. 4Ge1. 6 (PO4) 3 prepared by tape casting. J Alloy Compd 590:147–152

[23] Sebastiani M, Renzelli M, Battaini P, Bemporad E (2014) Focused ion beam and nanomechanical tests for high resolution surface characterisation: new resources for platinum group metals testing. Platin Met Rev 58(1):3–19

[24] Sebastiani M, Johanns K, Herbert EG, Carassiti F, Pharr GM (2015) A novel pillar indentation splitting test for measuring fracture toughness of thin ceramic coatings. Phil Mag 95(16–18):1928–1944

[25] Sebastiani M, Johanns K, Herbert EG, Pharr GM (2015) Measurement of fracture toughness by nanoindentation methods: Recent advances and future challenges. Curr Opin Solid State Mater Sci 19(6):324–333

[26] Thokchom JS, Kumar B (2010) The effects of crystallization parameters on the ionic conductivity of a lithium aluminum germanium phosphate glass–ceramic. J Power Sources 195(9):2870–2876

[27] Dashjav E et al (2020) Microstructure, ionic conductivity and mechanical properties of tape-cast Li1.5Al0.5-Ti1.5P3O12 electrolyte sheets. J Eur Ceram Soc 40(5):1975–1982

[28] Marder R, Chaim R, Chevallier G, Estournès C (2011) Effect of 1 wt% LiF additive on the densification of nanocrystalline Y2O3 ceramics by spark plasma sintering. J Eur Ceram Soc 31(6):1057–1066

[29] Luo W, Xie R, Ivanov M, Pan Y, Kou H, Li J (2017) Effects of LiF on the microstructure and optical properties of hot-pressed MgAl2O4 ceramics. Ceram Int 43(9):6891–6897

[30] Hao Y-Z, Yang H, Chen G-H, Zhang Q-L (2013) Microwave dielectric properties of Li2TiO3 ceramics doped with LiF for LTCC applications. J Alloy Compd 552:173–179

[31] Naqash S, Ma Q, Tietz F, Guillon O (2017) Na3Zr2 (SiO4) 2 (PO4) prepared by a solution-assisted solid state reaction. Solid State Ionics 302:83–91

[32] Dashjav E et al (2018) The influence of water on the electrical conductivity of aluminum-substituted lithium titanium phosphates. Solid State Ionics 321:83–90

[33] de Boer GB, de Weerd C, Thoenes D, Goossens HW (1987) Laser diffraction spectrometry: Fraunhofer diffraction versus Mie scattering. Part Part Syst Charact 4(1–4):14–19

[34] Yan G et al (2019) Anisotropy of the mechanical properties of Li1 3Al0 3Ti1 7 (PO4) 3 solid electrolyte material. J Power Sour 437:226940

[35] Wang A-N, Nonemacher JF, Yan G, Finsterbusch M, Malzbender J, Krüger M (2018) Mechanical properties of the solid electrolyte Al-substituted Li7La3Zr2O12 (LLZO) by utilizing micro-pillar indentation splitting test. J Eur Ceram Soc 38(9):3201–3209

[36] Zou Y, Malzbender J (2016) Development and optimization of porosity measurement techniques. Ceram Int 42(2):2861–2870

[37] Schneider CA, Rasband WS, Eliceiri KW (2012) NIH Image to ImageJ: 25 years of image analysis. Nat Methods 9(7):671–675

[38] Lauener CM, Petho L, Chen M, Xiao Y, Michler J, Wheeler JM (2018) Fracture of silicon: influence of rate, positioning accuracy, FIB machining, and elevated temperatures on toughness measured by pillar indentation splitting. Mater Des 142:340–349

[39] Kojima H, Whiteway S, Masson C (1968) Melting points of inorganic fluorides. Can J Chem 46(18):2968–2971

[40] Catti M (2001) A mixed α/β superstructure in NASICON ionic conductors: Neutron diffraction study of Li2FeTi (PO4) 3 and Li2FeZr (PO4) 3. J Solid State Chem 156(2):305–312

[41] Hirschorn B, Orazem ME, Tribollet B, Vivier V, Frateur I, Musiani M (2010) Determination of effective capacitance and film thickness from constant-phase-element parameters. Electrochim Acta 55(21):6218–6227

[42] Naqash S, Sebold D, Tietz F, Guillon O (2019) Microstructure–conductivity relationship of Na3Zr2 (SiO4) 2 (PO4) ceramics. J Am Ceram Soc 102(3):1057–1070

[43] Rettenwander D et al (2016) A microcontact impedance study on NASICON-type Li 1+ x Al x Ti 2–x (PO 4) 3 (0≤ x≤ 0.5) single crystals. J Mater Chem A 4(4):1506–1513

[44] Wolfenstine J, Allen JL, Sakamoto J, Siegel DJ, Choe H (2018) Mechanical behavior of Li-ion-conducting crystalline oxide-based solid electrolytes: a brief review. Ionics 24(5):1271–1276

[45] Wang JC (1984) Young's modulus of porous materials. J Mater Sci 19:801–808. https://doi.org/10.1007/BF00540451

[46] Phani KK, Niyogi S (1987) Young's modulus of porous brittle solids. J Mater Sci 22:257–263. https://doi.org/10.1007/BF01160581

[47] Fryxell R, Chandler B (1964) Creep, strength, expansion, and elastic moduli of sintered BeO as a function of grain size, porosity, and grain orientation. J Am Ceram Soc 47(6):283–291

[48] Ramakrishnan N, Arunachalam V (1990) Effective elastic moduli of porous solids. J Mater Sci 25:3930–3937. https://doi.org/10.1007/BF00582462